Controlling the Growth and Luminescence Properties of Well-Faceted ZnO Nanorods

ARTICLE *in* THE JOURNAL OF PHYSICAL CHEMISTRY C · MAY 2007

Impact Factor: 4.77 · DOI: 10.1021/jp071846t

Controlling the Growth and Luminescence Properties of Well-Faceted ZnO Nanorods

E. De la Rosa,[†] S. Sepúlveda-Guzman, B. Reeja-Jayan, A. Torres, P. Salas,[‡] N. Elizondo, and M. Jose Yacaman*

Department of Chemical Engineering and Texas Materials Institute, University of Texas at Austin, Austin, Texas 78712

Received: March 7, 2007; In Final Form: April 9, 2007

In this work, we synthesized ZnO nanorods by a wet chemical process. By varying different parameters of the synthesis process like precursor concentration, solvent used, surfactant, temperature, and reaction time, we were able to control the aspect ratio (l/d) and sharpness factor ($S_f = h/b$) of the rods. Rods with an aspect ratio of ∼20 and a sharpness factor of 10 were repeatedly obtained and characterized from scanning electron microscopy. High-resolution transmission electron microscopy and dark field analysis revealed that nanorods grow as a single crystal along the *c* axis [0001]. UV and visible emission was obtained in both flat- and sharp-terminated rods. According to the XPS analysis, rods present an excess of Zn^{2+} of ∼4% that is responsible for the strong yellow emission band. Such defects were removed by annealing of the sample at 200 °C for 2 h. Possible mechanisms of changes in the morphology produced by changes in the synthesis process are also discussed.

1. Introduction

Zinc oxide has been widely studied in the last years because of its excellent optical and electronic properties opening a bunch of potential applications in the future nano-optoelectronic industry such as, sensors,[1] UV lasers,[2] luminescent phosphor,[3] photonic crystals,[4] solar cells,[5] hydrogen storage,[6] and field emitters,[7] to mention a few. ZnO is a direct band gap semiconductor with a room-temperature wide band gap of 3.37 eV and a large excitonic (electron−hole) binding energy of 60 meV, larger than thermal energy at room temperature (26 meV). This difference in the binding energy combined with an efficient excitonic recombination forms the basis of room-temperature lasing of ZnO. Recently, UV lasing was reported with a threshold power density as low as 40 kW/cm^2 for a directionally grown nanorod array, much lower than the threshold for polycrystalline powder and GaN with a binding energy of 25 meV.[2] Nanorods act individually as excellent optical waveguides due to the difference in the refractive index between ZnO (n = 2.45) and air (n = 1.00), with the stimulated emission finally being emitted from the plane face of nanorods. Lasing performance of the nanorods depends not only on an efficient gain medium but also on the surface quality, the reflectivity formed for the end-face of the rod, and the aspect ratio (l/d) determined for the length and diameter of the rod. Controlling the aspect ratio is also very important for efficient field emission applications such as field emission flat panel displays.[8] The quality of the nanorods also affects the luminescence properties. The characteristic emission band of ZnO is centered at 390 nm and is attributed to the free exciton recombination. A green emission band centered at 520 nm was also reported and has been associated with the recombination of a photogenerated hole with the single ionized charge state of the single ionized oxygen vacancy.[3] Such oxygen deficiency has also been observed in microcrystals, and in both cases, defects are on or very close to the surface of the nanorods. Recently, it has been reported that nanostructures also present a broad orange band centered at 620 nm.[9] The most accepted explanation of this emission band is that it is produced by defects such as an excess of oxygen in the nanostructure. Both visible bands make ZnO a very attractive low-voltage phosphor for field emission displays. The enhancement of one band is at the expense of the other visible bands. Both types of defects are produced during the synthesis process but, in general, are not fully controlled (not only their presence but also their density). Furthermore, those defects can change from one batch to another one.

Controlling the synthesis process in order to select and control the presence of specific defects is a challenge and is a very important subject of research around the world. Zinc oxide nanorods have been synthesized by different physical and chemical methods. Physical methods like vapor-phase,[10,11] molecular beam epitaxy,[2] thermal reduction,[12] pyrolysis,[13] and microwaves[14] have all been successfully used in the production of nanorods and other different morphologies. However, these methods require high temperature, a complex procedure, and sophisticated equipment that make it expensive, thereby restricting possibilities of applications. Low-temperature wet chemical processes such as precipitation, hydrolysis, and the hydrothermal process are widely used in the synthesis of a wide variety of ZnO nanostructures.[15−17] These methods are economical and suitable for large-scale production. ZnO nanorods have been successfully synthesized by the hydrothermal process.[8,17,18] According to previous work, the synthesis of ZnO rods is based on the decomposition of $Zn(OH)_4^{2-}$ and $Zn(NH_3)_4^{2+}$, but the final product is very sensitive to reaction parameters such as chemical reagents, pH, and the annealing process.[19] Systematic studies about the effect of the reaction parameters on the morphology of the resulting ZnO structure have been reported. However, the correlation between the synthesis conditions, the morphology, and the luminescence properties of the ZnO

* To whom correspondence should be addressed. E-mail: yacaman@che.utexas.edu. Tel.: (512) 232-9111. Fax: (512) 475-8090.

[†] On sabbatical from Centro de Investigaciones en Optica, León, Gto. 37150 México. E-mail: elder@cio.mx.

[‡] Instituto Mexicano del Petroleo, Cd. de Mexico, D.F., 07730 México.

10.1021/jp071846t CCC: $37.00
Published on Web 05/27/2007

TABLE 1: Summary of the Reaction Conditions

sample	H_2O/ethanol (vol %)	surfactant (wt %)	temperature (°C)
S1a[a]	1:0		100
S1b	1:0		100
S1c	1:0		200
S2	0.8:0.2		100
S3	0.8:0.2	0.5	100
S4	1:0	0.5	100

[a] In this case, the reactant concentration was reduced, keeping the ratio $Zn(NO_3)_2$/NaOH constant.

nanorods still remains unclear and demands better explanation. In this work, we report the systematic characterization of ZnO nanorods prepared by hydrothermal method by studying the growth mechanism, the control of the aspect ratio (l/d), the sharp termination, and their correlation with the luminescence properties. We propose a procedure to control the aspect ratio and defects associated with a deficiency and excess of oxygen in the ZnO nanorods. This, in turn, will help to control the luminescence properties of these nanorods.

2. Experimental Procedures

All reagents, including zinc nitrate ($Zn(NO_3)_2 \cdot 6H_2O$), sodium hydroxide (NaOH), and hexadecyltrimethyl ammonium bromide (CTAB), were analytical grade purchased from Aldrich and used as received. In a typical procedure, 8 mL of 4 M NaOH solution was added to 16 mL of deionized water under magnetic stirring, and then, 8 mL of 0.2 M $Zn(NO_3)_2 \cdot 6H_2O$ solution was added. The solution was stirred for 10 min, and then, 7 mL of the mixture was transferred into a Teflon-lined stainless steel autoclave with a capacity of 25 mL. The autoclave was sealed and kept under heating for 6 h. Table 1 summarizes the reaction parameters used in the different cases, where CTAB (0.5 wt %), ethanol (20 vol %), or both of them were introduced to control the morphology of the ZnO nanostructure. After the reaction was completed, the mixture was cooled at room temperature, and the white powder was separated from the solution by centrifugation and washed with deionized water and ethanol. Finally, the product was kept dispersed in ethanol.

The morphology of the nanorods was analyzed by scanning electron microscopy (SEM) using a Hitachi S-4500II operating at 10 kV. Transmission electron microscopy (TEM), high-resolution transmission electron microscopy (HRTEM), high-angle annular dark field (HAADF), dark field (DF), selected area diffraction (SAD), and energy dispersive X-ray spectroscopy (EDS) were performed on a Philips Tecnai F20 and JEOL 2010F at 200 kV. Samples were dispersed in ethanol at room temperature and sonicated for 10 min. Aliquots were dropped on 3 mm diameter lacey carbon copper grids. The X-ray diffraction (XRD) patterns were obtained using SIEMENS D-5005 equipment provided with a Cu tube with Kα radiation at 1.5405 Å, scanning in the 30−70° 2θ range with increments of 0.03°, and a sweep time of 8 s. The samples were analyzed by X-ray photoelectron spectroscopy (XPS) on a PHI 5700 system equipped with dual Mg X-ray source and monochromated Al X-ray source with depth profile and angle-resolved capabilities. The charging effect was corrected by shifting the binding energies, considering the C 1s signal at 284.6. Nonlinear fit, using Gaussian−Lorentzian curves, was performed, maintaining the full-width at half-maximum (fwhm) constant for all components in a particular spectrum. The photoluminescence (PL) characterization was performed at room temperature on a Jovin Yvon fluorometer under 350 nm excitation from a 75 W UV Xe lamp. ZnO powder was dispersed in solution into a quartz cuvette. All spectra presented here are corrected for cuvette, solvent emission, and for the electronic noise. Correction was performed measuring the response of each component, and then, the difference was taken mathematically. The scattering problem was minimized, keeping the solution in the cuvette at rest for a while.

3. Results and Discussion

3.1. Chemical Reaction. On the basis on the above-described hydrothermal process, ZnO was obtained. During the reaction, the $Zn(OH)_2$ was immediately formed when the NaOH solution was added. However, it was dissolved because of the final high ratio $[OH^-]/[Zn^{2+}]$ in the resultant solution that, in our case, was 20. Under these reaction conditions, the conversion of $Zn(OH)_2$ to $Zn(OH)_4^{2-}$ occurred as is shown by the following equations

$$Zn^{2+} + 2OH \rightarrow Zn(OH)_2 \quad (1)$$

$$Zn(OH)_2 + H_2O \rightarrow Zn(OH)_4^{2-} + 2H^+ \quad (2)$$

Gradually, under the thermal conditions, the reaction between the $Zn(OH)_4^{2-}$ species leads to form large zinc hydroxide species $Zn_xO_y(OH)_z^{(z+2y-2x)}$, which finally precipitate and form the ZnO, as is described by the following equation

$$Zn(OH)_4^{2-} + Zn(OH)_4^{2-} \rightarrow Zn_2O(OH)_6^{4-} + H_2O \quad (3)$$

This reaction mechanism has been widely explained recently by S. Yamabi et. al.[20] and W. J. Li et. al.[21] When ethanol is added, changes in the OH^- concentration and the pressure of the hydrothermal condition are expected. These changes affect the kinetics parameters of the reaction process due to the solubility of the intermediate products, and the morphology of ZnO is effected. On the other hand, the effect of CTAB on the synthesis of ZnO depends on the formation of a complex between the CTAB and the ions in the reaction media. Because CTAB is a cationic surfactant, the formation of a complex with the OH^- ion is easier than that with Zn^{2+} ions. Then, CTAB can be adsorbed on the ZnO surface, affecting the growing mechanism. As a consequence, a strong effect in the morphology is expected when CTAB is used as an additive.

3.2. Morphology Characterization (SEM). The morphology and average size of the nanorods were studied from SEM and STEM micrographs. Well-faceted hexagonal rods were observed. Figure 1 shows the SEM images of set S1 (S1a, S1b, and S1c). The average size of the rods for S1a and S1b is 600 nm in diameter and 11 μm length, indicating an aspect ratio (l/d) of 18; for S1c, the length is 14 μm and diameter 750 nm, indicating an aspect ratio of 18. The temperature increment enhances the growth of the rods, keeping the aspect ratio constant. As was discussed for other authors, as the aspect ratio is increased, both optical and field emission properties are enhanced. Notice that for the S1b sample, both ends of the rods are flat, while S1a has a sharp (prismatic or pyramidal) termination. Then, the sharpness factor can be defined as the ratio of the pyramid's height to the size of the top flat surface ($S_f = h/b$). The sharpness factor for S1a is ~1.6, while for S1c, it is ~11. These results suggest that the low pH value of the solution ($pH_{S1a} = 10.5$ and $pH_{S1b} = 11$) induces the sharp termination of the rods, and the annealing temperature enhances it ($T_{S1a} = 100$ °C and $T_{S1c} = 200$ °C). Because the increment of temperature means an increment of the pressure, it can be concluded that the dominant parameter promoting the sharp

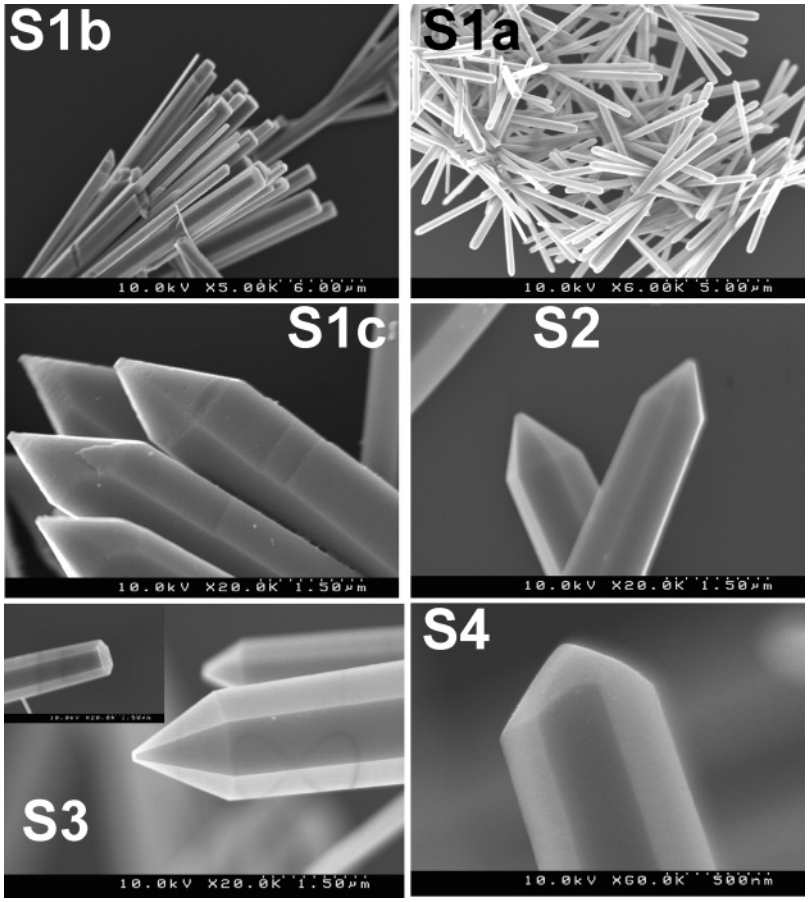

Figure 1. Typical SEM images for all prepared samples.

termination is the pressure. This hypothesis was confirmed with the addition of alcohol (S2 sample); in this case, the top flat surface of the pyramid was only 70 nm, but the height was diminished, keeping the sharpness factor similar to that of S1c. A change in the kinetics promotes a strong radial growth, reducing the aspect ratio of the rods (∼9). This unproportional growth can explain the reduction of the pyramid's height. The introduction of surfactant controls the lateral growth, reducing the diameter to 0.8 μm, half of the diameter obtained for samples prepared with only alcohol, thereby enhancing the aspect ratio to ∼20 with a sharpness factor of ∼10. However, it is also possible to observe rods with flat or poor sharp termination; see Figure 1c. Rods with only flat or poor sharp termination were obtained when the sample was synthesized with surfactant but no alcohol (S4 sample).

3.3. Structural Characterization (HRTEM, STEM, SAD). The crystalline phase presented for all samples is the wurzite structure (hexagonal with space group $P_6 3mc$), as was confirmed by XRD. The corresponding XRD pattern for S2 is presented in Figure 2. All diffraction peaks were indexed and are in agreement with JCPDS 36-1451. From these patterns, lattice parameters were calculated, obtaining $a = 3.250$ Å and $c = 5.208$ Å for S1c and S2. Such values are in agreement with the standard parameter for the wurzite crystalline structure, $a = 3.253$ Å and $c = 5.213$ Å. Characteristic TEM, HAADF, and high-resolution and FFT micrographs are shown in Figure 3. In this figure, the flat and sharp termination was confirmed; see Figure 3a and b. The HAADF image does not show any stacking defects in the crystalline structure, suggesting the good quality of the crystal. From here, EDS analysis was performed, indicating that only Zn and O atoms are present in the ZnO rods; no other element was observed. The high-resolution image,

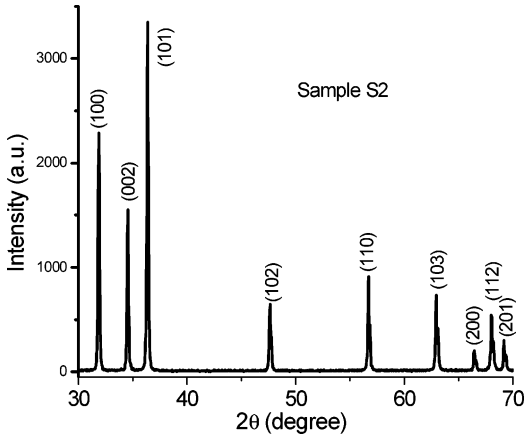

Figure 2. XRD pattern for the S2 sample.

see Figure 3c, suggests that the growth of ZnO is along the *c* axis corresponding to the [0001] direction. The SAD pattern acquired from sample S2, see Figure 4 at the center, shows that the growth direction of the rods is the *c* axis, which is in correspondence with the dark field image shown in Figure 4a. No linear defects were observed according to SAD, as is shown in Figure 4b−d, indicating that a single crystal was grown. ZnO is a hexagonal polar crystal, and the *c* axis, the preferential growing direction, is the polar axis. As was discussed above, the basic block to construct the crystal is the complex $Zn(OH)_4$. These basic building blocks are bonded together under a condensation reaction, producing the nuclei $[Zn_xO_y(OH)_z]$, where nucleation process occurs. The resulting ZnO is composed of tetrahedrons that share an edge, face, and corner. In the internal part of the crystals, tetrahedra are connected by sharing oxygen,

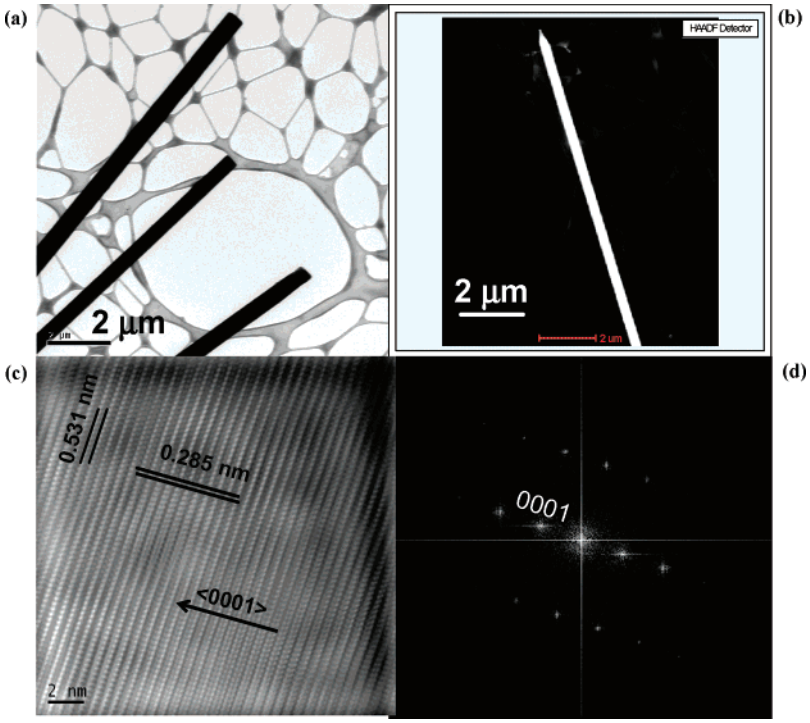

Figure 3. (a) TEM image of flat terminated rods (S1a) and (b) HAADF image for the S2 sample; in both cases, the scale bars represent 2 μm. (c) HRTEM image for the S1a sample; (d) the corresponding FFT pattern.

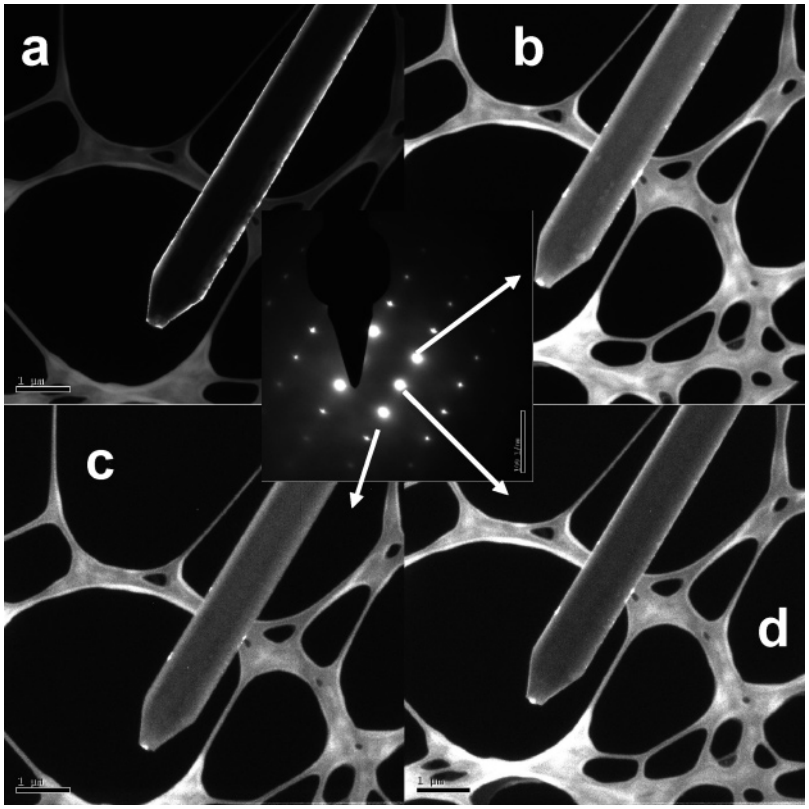

Figure 4. Dark field micrograph for the S2 sample. In the center is the SAD pattern corresponding to the TEM image in (a). The micrograph obtained from the different diffraction spots, as indicated, shows a high-quality single crystal with a smooth surface.

but in the interface, the terminal vertex is an OH^-, as has been proved by FTIR and Raman spectroscopy.[22,23] The OH^- terminations are preferentially distributed along the *c* axis, and then, the edge and face termination are perpendicular, obeying the polar condition of the crystal. The growth habit or morphology of the crystals depends on the relative growth rate of the different faces of the crystal, which in turn, depends on their interface structure.[21] Figure 5 shows a schematic diagram of both flat and sharp or prismatic-terminated rods characteristic of the sample under study. The growth rate along the radial axis should be a little higher or at least equal to that along the *c* axis, that is, $V[01\bar{1}0] \geq V[0001]$.[21] This compensates for the

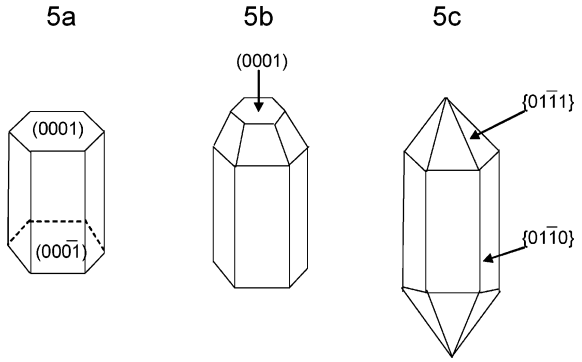

Figure 5. Schematic diagram of rods with different ends, in agreement with obtained ZnO rods.

high content of OH^- termination along the *c* axis and keeps the rod very uniform, well-faceted, and with both terminations flat; see Figure 5a.

The changes in the pH induce changes in the kinetic parameters than, in turn, can change the morphology. In our study, pH was modified by changing the concentration of the reactants, keeping the concentration ratio $Zn(NO_3)_2$/NaOH constant and the same reaction volume. The sample S1b (flat termination) had a higher concentration of $ZnO(OH)^-$ than S1a (one side prismatic termination). The depletion of building blocks in combination with the polar property changes the velocity growth relation and explains the prismatic termination of the rods. In this case, $V[0001] > V[01\bar{1}1] > V[01\bar{1}0]$; see Figure 5b. This is in agreement with the idealized growth habit reported before.[21] The polar condition of the crystal induces building blocks to be aligned mainly along the *c* axis, reducing the growth rate along the radial axis. The kinetic parameters can also be changed by changing the temperature or pressure of the synthesis process. The increment in temperature increases the mobility of the building blocks $ZnO(OH)^-$ and then accelerates the condensation process. Here again, the polar condition of the crystal promotes higher accumulation along the *c* axis, which explains the sharp termination of rods observed in the sample S1c; see Figures S1c and 5c. The prismatic termination of both ends of the rods suggest that the increment in temperature, which means the increment of pressure, strongly increases the growth rate along the *c* axis V[0001]. However, a higher increment in the pressure promotes radial growth, instead of infinitely increasing the growth velocity. This was observed when alcohol was added to the reaction mixture (sample S2). As was expected and described above, the diameter of the rods was increased, while the prismatic termination was maintained. In the case where the surfactant (CTAB) was added (sample S3), the diameter was reduced almost to half of the diameter obtained without any surfactant (sample S2). One possible explanation of this process is that the surfactant is bonded to the edge or face termination of the rods, reducing the radial growth, and as a consequence, the longitudinal growth is promoted. These observations are in agreement with those reports where the radial growth on ZnO rods is controlled by using surfactant.[8] The overall result is an increment of the aspect ratio of the obtained rods, as was discussed above. The price paid for such enhancement is a little reduction of the sharpness factor, from 11.5 to 10, and the appearance of rods with one flat end. As was discussed above, synthesis using surfactant but no alcohol (S4 sample) strongly reduces both the aspect ratio and the sharpness factor of the rods. This confirms that pressure and the right concentration of CTAB play a very important role in the rod synthesis controlling the rods' growth and both the aspect ratio and the sharpness factor.

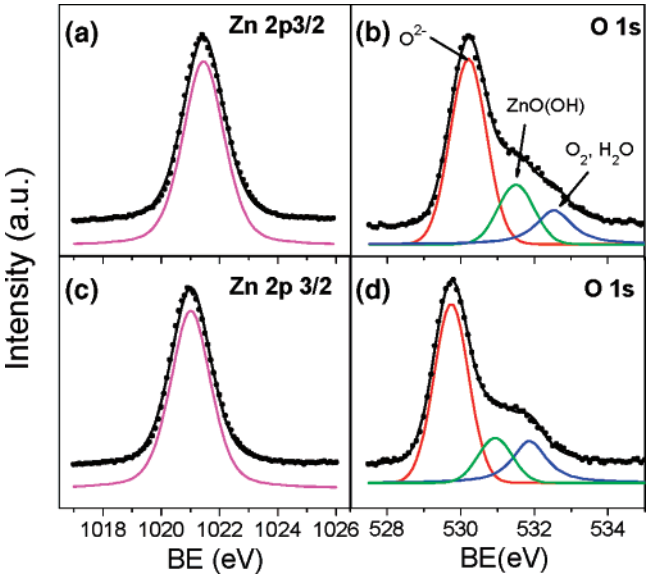

Figure 6. (a) Zn $^2p_{3/2}$ and (b) O1s spectra of the S1c sample and (c) Zn $^2p_{3/2}$ and (d) O1s spectra of the S3 sample.

3.4. XPS Characterization. The XPS analysis of the S1c and S3 samples was performed in order to investigate chemical composition. Figure 6a and c show the XPS spectra for the Zn $^2p_{3/2}$ core level for the S1c and S3 samples, respectively. In both cases, there is only one peak with a binding energy of 1021.4 eV associated to Zn in the completely oxidized state.[7,24−26] The deconvolution of the XPS spectra for the O 1s core level line is shown in Figure 6b and d for S1c and S3, respectively. The deconvolution of those bands shows the presence of three different peaks. The dominant peak centered at 530.20 eV (O1) is associated to the O^{2-} ion in the wurzite structure surrounded by the Zn atoms with their full complement of nearest-neighbor O^{2-} ions.[7,25−27] The peak at 531.50 eV (O2) is associated with the O^{2-} ion in the zinc oxyhydroxide species, ZnO(OH), in oxygen-deficient regions within the matrix of ZnO.[7] This component has been identified for other oxyhydroxides with a binding energy similar to the one reported here.[28] The binding energy peak at 532.5 eV (O3) is associated with the presence of loosely bound oxygen such as CO_3, adsorbed O_2, or adsorbed H_2O on the ZnO surface.[25,27] The relative atomic concentration was calculated from the area of different peaks and by considering a sensitivity factor of 21.734 for Zn and 5.148 for O. The ratio O1/Zn was ∼0.77 for both S1c and S3, indicating that only 77% of Zn atoms are bonded to O^{2-} as ZnO. This result suggests a 23% deficiency of the O^{2-} ion (and therefore, the free Zn ion) within the matrix of ZnO. The ratio O2/Zn was ∼0.23 for the S1c sample, confirming that 23% of free Zn^{2+} is forming the ZnO(OH) oxyhydroxide. This means that O1/Zn + O2/Zn = 1 indicates that all Zn atoms are bonded in ZnO or ZnO(OH) species. Thus, no excess of Zn should be observed. However, for the S3 sample, the ratio O2/Zn was ∼0.19, indicating that, in this case, only 19% was forming the oxyhydroxide ZnO(OH). This result suggests a 4% excess of Zn^{2+} in the matrix of ZnO, leading to the formation of suboxide species (ZnO_x, $x < 1$). In addition, the concentration of oxygen species adsorbed on the ZnO surface (O3/O1) was ∼0.23 and ∼0.16 for the S1c and S3 samples, respectively. This difference is probably produced because the sample S1c was prepared in an aqueous media.

3.5. Photoluminescence Characterization. The photoluminescence of all prepared ZnO samples was performed and characterized as a function of the synthesis procedure. The

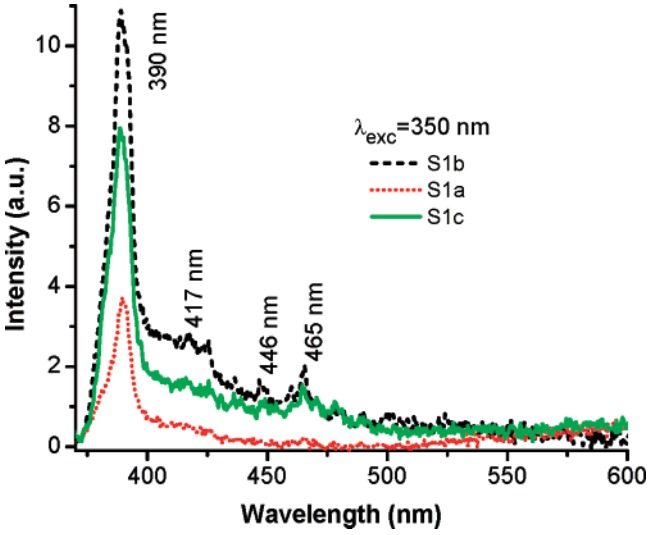

Figure 7. Room-temperature PL spectra of ZnO nanorods for set S1.

luminescence spectra for sample set S1 are shown in Figure 7. The dominant band is the characteristic near band gap (NBG) emission centered at 390 nm and ascribed to the free recombination of excitons. Such emission is in correspondence with the emission band reported in the literature. The difference in the UV signal intensity in the different samples was produced by the density of rods in the solution, which in turn, is related to the rod size. In fact, a solution of sample S1a was much more transparent to the naked eyes, indicating lower rod concentration, in agreement with the synthesis using a reduced concentration. In addition to the UV band, a broad shoulder (400−425 nm) and weak peaks at 417, 446, and 465 nm were observed. These blue bands have been observed before in nanostructured ZnO, but in this work, they are well defined.[29] The blue bands have been ascribed to electron transition from the shallow donor level of oxygen vacancies ($\Delta E_g = \sim 2.8$ eV) and the zinc interstitial ($\Delta E_g = \sim 2.7$ eV) to the valence band.[30] Both oxygen vacancies and the zinc interstitial were probably formed during the synthesis process due to the kinetics parameters. In fact, ZnO tends easily to lose oxygen, becoming nonstoichiometric, in part, due to the low energy ($E = \sim 3$ eV) required to break the oxygen bond. The low intensity of those peaks indicates the low density or luminescent recombination efficiency of such defects. Notice the evanescent decay of the signal emitted as a result of the dispersion produced by the colloidal nanorods.

The PL spectra of the S2−S4 samples are shown in Figure 8. The luminescence was dominated by a very strong broad yellow emission band centered at 580 nm. Previous studies on ZnO have reported green emission (~520 nm) and others an orange emission (~620 nm) band.[9,31] The red shift of the emission band reported here indicates that those defects producing the orange emission are dominant. Notice that the weak peak at 465 nm, described above as associated to oxygen deficiency, is present in all cases, confirming that the defect is not related to the presence of alcohol and surfactant. This band deserves special attention because its combination with the yellow band can produce white light that is very important for solid-state lighting and field emission displays. The ratio between the integrated signals of the UV and visible bands (I_{UV}/I_{vis}) is 0.7, 0.8, and 2.8 for S2, S3, and S4, respectively. This suggests that the alcohol, in the synthesis process, is the main promoter of defects producing visible emission. Figure 8b shows, in detail, the visible band of samples S2 and S3. It is clearly observed that the introduction of surfactant (sample S3)

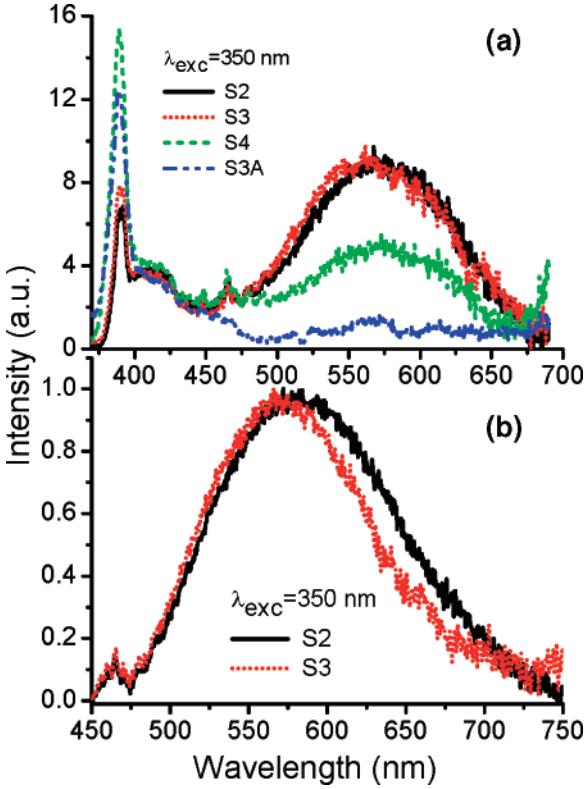

Figure 8. Room-temperature PL spectra of ZnO nanorods for (a) UV−vis emission and (b) visible emission; the S3A plot corresponds to the PL of sample S3 annealed at 200 °C for 2 h.

induces a little UV shift of the signal, in part, produced by the quenching of the red side of the emission. Although a shoulder at 643 nm was formed, these differences could be the result of a kind of competition of the type of defect formed. Furthermore, a strong quenching of the yellow emission was observed for the sample prepared with surfactant (but no alcohol), the NBG UV emission band being dominant. A detailed analysis shows little changes in the structure of the visible signal, in particular, a well-defined shoulder at 610 nm. Although the surfactant preferentially promotes defects associated to the red side of the emission, the overall result is the promotion of defects emitting in the visible, which means a deterioration of the UV signal. Thus, the introduction of CTAB in the absence of alcohol in the synthesis process not only destroys the control of aspect ratio and sharp termination of the rods but also quenches the signal emitted. However, in combination with alcohol, it is possible to control the aspect ratio and sharpness factor of the rods, keeping a very strong visible signal.

The origin of visible emission is controversial, and different hypotheses have been proposed to explain both the green and orange emission bands. The green emission has been associated to single ionized oxygen vacancies, oxygen antisites, zinc vacancies, and oxygen deficiency.[31−34] The orange emission has been associated to an excess of oxygen, interstitial zinc, and impurities like Li ions.[9,32] Recently, it has been proposed that the presence of $Zn(OH)_2$ on the surface is responsible for both green and orange emission.[35] The most probable is that visible emission could be produced by the combination of different kinds of defects, depending of every specific preparation method. In order to elucidate the origin of those defects producing visible emission, the sample S3 was annealed at 200 °C for 2 h; after that, the PL was measured and is shown in Figure 8a. Experimental results indicate that visible emission was almost completely quenched. Notice that even the peak at

465 nm disappeared. Some weak peaks can be observed, indicating that some defects still exist in the crystalline structure. The remnant peaks should be associated to those defects that require a different process to be removed, probably the excess of oxygen in the bulk that is removed only in a forming atmosphere, as was reported recently.[9,31] According to these results, we conclude that the yellow emission is associated with the zinc interstitial close to or on the surface of the structure. This assumption is supported by the XPS results; see Figure 6. After the annealing process, the XPS result showed that the ratio O1/Zn was increased from 77 to 83%, indicating an increment of O1 species or more $ZnO(OH)_2$ converted to ZnO, while the ratio O2/Zn was still 19% forming oxyhydroxide. These results indicate that the excess of Zn^{2+} was completely removed. This means that the absence of an excess of Zn does not produce a visible emission band. This can be corroborated by considering that sample S1c with 0% of Zn excess does not present a visible band. Furthermore, the annealing of the sample was performed in an oxidant atmosphere; therefore, an excess of Zn^{2+} can be easily oxidized and is in agreement with results reported by other authors.[9,31] Zinc interstitials have lower formation energy, while zinc vacancies require higher energy that reduces the formation probability.[30] Considering the evidence described above, we conclude that the yellow emission band was produced by the excess of Zn^{2+} and was not due to the presence of oxyhydroxide.

4. Conclusions

According to experimental results from XPS, it is possible to obtain nanorods with flat and a very sharp termination and no defects (or at least a very low concentration) associated with nonstoichiometric composition. This is also confirmed by the absence of visible emission. Electron microscopy does not show stacking evidence, indicating that the nanorods are single crystals. The obtained aspect ratio, ~20, in combination with the sharpness factor can improve properties, especially for lighting and field emission applications, and the sharpness factor (S_f) can be useful as a metric for the quality of the tip. Experimental results show that alcohol improves the sharp termination of the rods and, in combination with the surfactant, improves the aspect ratio. Thus, the right concentration of both guarantees good balance of both factors. In the absence of intrinsic defects, a deficiency of oxygen, the presence of oxyhydroxide, and probably some excess of oxygen, exciton recombination is the only relaxation channel. This means the UV emission band can be maximized. Defects are not associated with the sharp termination of rods but are associated with changes in the kinetics during the synthesis process. Apparently, defects are associated with an increment of the kinetic parameters that increase the condensation process. Controlling the condensation mechanism helps to control the density of defects, making it possible to control the intensity of the yellow emission. This opens up a lot of possibilities for solid-state lighting and displays. XPS results corroborate that the yellow band was produced by the presence of an excess of the Zn^{2+} ion.

Acknowledgment. The authors are indebted to DARPA (HR011-06-1-005), the Welch Foundation (Grant F-1615), and SPRING for financial support of this work. E.D.L.R. wants to acknowledge CIO for its support. We thank Dr. Y. Sun for XPS measurements and Dr. X. Gao for TEM assistance.

References and Notes

(1) Wang, H. T.; Kang, B. S.; Ren, F.; Tien, L. C.; Sadik, P. W.; Norton, D. P.; Pearton, S. J. *Appl. Phys. Lett.* **2005**, *86*, 243503.
(2) Huang, M. H.; Mao, S.; Feick, H.; Yan, H.; Wu, Y.; Kind, H.; Weber, E.; Russo, R.; Yang, P. *Science* **2001**, *292*, 1897.
(3) Vanheusden, K.; Warren, W. L.; Seager, C. H.; Tallant, D. R.; Voigt, J. A.; Gnade, B. E. *J. Appl. Phys.* **1996**, *79*, 7983.
(4) Wang, X.; Neff, C.; Graungnard, E.; Ding, Y.; King, J. S.; Pranger, L. A.; Tannenbaum, R.; Wang, Z. L.; Summers, C. J. *Adv. Mater.* **2005**, *17*, 2103.
(5) Law, M.; Greene, L. E.; Johnson, J. C.; Saykally, R.; Yang, P. *Nat. Mater.* **2005**, *4*, 455.
(6) Wan, Q.; Lin, C. L.; Yu, B.; Wang, T. H. *Appl. Phys. Lett.* **2004**, *84*, 124.
(7) Ramgir, N. S.; Late, D. J.; Bhise, A. B.; More, M. A.; Mulla, I. S.; Joag, D. S.; Vijayamohanan, K. *J. Phys, Chem. B* **2006**, *110*, 18236.
(8) Dev, A.; Panda, S. K.; Kar, S.; Chakrabarti, S.; Chaudhuri, S. *J. Phys. Chem. B* **2006**, *110*, 14266.
(9) Hsu, J. W. P.; Tallant, D. R.; Simpson, R. L.; Missert, N. A.; Copeland, R. G. *Appl. Phys. Lett.* **2006**, *88*, 252103.
(10) Wu, J. J.; Liu, S. C. *Adv. Mater.* **2002**, *14*, 215.
(11) Dai, Z. R.; Pan, Z. W.; Wang, Z. L. *Adv. Funct. Mater.* **2003**, *13*, 9.
(12) Hu, J. Q.; Li, Q.; Meng, X. M.; Lee, C. S.; Lee, S. T. *Chem. Mater.* **2003**, *15*, 305.
(13) Wu, J. J.; Liu, S. c.; Wu, C. T.; Chen, K. H.; Chen, L. C. *Appl. Phys. Lett.* **2002**, *81*, 1312.
(14) Zhang, X. H.; Xie, S. Y.; Jiang, Z. Y.; Zhang, X.; Tian, Z. Q.; Xie, Z. X.; Huang, R. B.; Zheng, L. S. *J. Phys. Chem. B* **2003**, *107*, 10114.
(15) Iwasaki, M.; Inubushi, Y.; Ito, S. *J. Mater. Sci. Lett.* **1997**, *16*, 1503.
(16) Jezequel, D.; Guenot, J.; Jouini, N.; Fievet, F. J. *J. Mater. Res.* **1995**, *10*, 77.
(17) Yang, M.; Pang, G.; Jiang, L.; Feng, S. *Nanotechnology* **2006**, *17*, 206.
(18) Pal, U.; Santiago, P. *J. Phys. Chem. B* **2005**, *109*, 15317.
(19) Zhang, J.; Sun, L.; Yin, J.; Su, H.; Liao, C.; Yan, C. *Chem. Mater.* **2002**, *14*, 4172.
(20) Yamabi, S.; Imai, H. *J. Mater. Chem.* **2002**, *12*, 3773.
(21) Li, W. J.; Shi, E. W.; Zhong, W. Z.; Yin, Z. W. *J. Cryst. Growth* **1999**, *203*, 186.
(22) Slunecko, J.; Kosec, M. *J. Am. Ceram. Soc.* **1998**, *81*, 1121.
(23) Dutta, P. K.; Gallagher, P. K.; Twa, J. *Chem. Mater.* **1992**, *4*, 847.
(24) Islam, M. N.; Ghosh, T. B.; Chopra, K. L.; Acharya, H. N. *Thin Solid Films* **1996**, *280*, 20.
(25) Chen, M.; Wang, X.; Yu, Y. H.; Pei, Z. L.; Bai, X. D.; Sun, C.; Huang, R. F.; Wen, L. S. *Appl. Surf. Sci.* **2000**, *158*, 134.
(26) Ye, J. D.; Gu, S. L.; Qin, F.; Zhu, S. M.; Liu, S. M.; Zhou, X.; Liu, W.; Hu, L. Q.; Zhang, R.; Shi, Y.; Zheng, Y. D.; Ye, Y. D. *Appl. Phys. A* **2005**, *81*, 809.
(27) Coppa, B. J.; Davis, R. F.; Nemanich, R. J. *Appl. Phys. Lett.* **2003**, *82*, 400.
(28) McIntyre, N. S.; Zetaruk, D. G. *Anal. Chem.* **1977**, *49*, 1521.
(29) Du, G. H.; Xu, F.; Yuan, Z. Y.; Tendeloo, G. V. *Appl. Phys. Lett.* **2006**, *88*, 243101.
(30) Zhang, D. H.; Xue, Z. Y.; Wang, Q. P. *J. Phys. D: Appl. Phys.* **2002**, *35*, 2837.
(31) Tam, K. H.; Cheung, C. K.; Leung, Y. H.; Djurisic, A. B.; Ling, C. C.; Beling, C. D.; Fung, S.; Kwok, W. M.; Chan, W. K.; Philips, D. L.; Ding, L.; Ge, W. K. *J. Phys. Chem. B* **2006**, *110*, 20865.
(32) Studenikin, S. A.; Golego, N.; Cocivera, M. *J. Appl. Phys.* **1998**, *84*, 2287.
(33) Li, D.; Leung, Y. H.; Djurisic, A. B.; Liu, Z. T.; Xie, M. H.; Shi, S. L.; Xu, S. J.; Chan, W. K. *Appl. Phys. Lett.* **2004**, *85*, 1601.
(34) Kwok, W. M.; Djurisic, A. B.; Leung, Y. H.; Chan, W. K.; Phillips, D. L. *Appl. Phys. Lett.* **2005**, *87*, 223111.
(35) Zhou, H.; Alves, H.; Hofmann, D. M.; Kriegseis, W.; Meyer, B. K.; Kaczmarczyk, G.; Hoffmann, A. *Appl. Phys. Lett.* **2002**, *80*, 210.